Journal of Inorganic and General Chemistry
ZAAC
Zeitschrift für anorganische und allgemeine Chemie
www.zaac.wiley-vch.de
RESEARCH ARTICLE

Check for updates

DOI: 10.1002/zaac.202300146

# Structural and magnetic properties of antifluorite-type $Li_{5+x}Fe_{1-x}Co_xO_4$

Rasmus Vester Thøgersen,[a] Asbjørn Slagtern Fjellvåg,[a] Øystein Slagtern Fjellvåg,[b, c] and Helmer Fjellvåg*[a]

*This work is inspired by earlier works by the late Professor Rudolf Hoppe and his co-workers, and the publication is therefore dedicated to him on the occasion of his 100th birthday in 2022.*

We report on the structural and magnetic properties of $Li_{5+x}Fe_{1-x}Co_xO_4$ ($0 \leq x \leq 1$). < The system assumes two distinct crystal structures at room temperature (α and β), and shows a transition in preference from α to β between $x = 0.18$ and $x = 0.25$. This tendency is supported by DFT-calculations. Upon heating, $Li_5FeO_4$ undergoes a reconstructive transition from α→β at ~1060 K, while $Li_6CoO_4$ shows an order-disorder transition from β→ε at ~885 K, where ε is a cubic cation-disordered antifluorite structure. $Li_{5.50}Fe_{0.50}Co_{0.50}O_4$ is stabilised towards the ordered β-phase until at least 1170 K. XANES-measurements confirm that the oxidation states of Fe and Co remain unchanged throughout the series with charge compensation from additional $Li^+$ on increasing *x*. Magnetic measurements show onset of low-temperature antiferromagnetic ordering around 3 K to 12 K. The magnetic structure of $Li_5FeO_4$ is described on the basis of powder neutron diffraction at 1.5 K, while the magnetic structures of $Li_{5.50}Fe_{0.50}Co_{0.50}O_4$ and $Li_6CoO_4$ are found to be slightly incommensurate below the ordering temperature.

## 1. Introduction

In the early 1970s, Demoisson *et al.* first reported the successful synthesis of $Li_5FeO_4$,[1] which was followed up and elaborated on in the 1980s by Luge and Hoppe.[2] The latter two also later reported the successful synthesis of $Li_6CoO_4$,[3] ensuring two new entries into a growing family of alkali metal ferrates and cobaltates that were discovered during that time. These are different variants of the antifluorite structure, and were denoted the α- and β-phases. They are essentially defect $Li_2O$-variants, both containing tetrahedrally coordinated transition metal ions charge compensated by Li-vacancies: two per $Fe^{3+}$ in $Li_5FeO_4$ and one per $Co^{2+}$ in $Li_6CoO_4$. They have also been dubbed island structures owing to the isolation of each transition metal tetrahedron within the unit cells. These Li-compounds differ from their Na-analogues, first reported some years preceding Hoppe and Luge's work on $Li_5FeO_4$ and $Li_6CoO_4$.[4,5] Although the crystal structure of the Na-analogues of $Li_5FeO_4$ and $Li_6CoO_4$, previously denoted as the γ-phase by the current authors,[6] is also derived from the antifluorite structure, it is severely distorted and deviates strongly from the ideal cubic structure. Furthermore, the existence of the direct Na-analogue of $Li_6CoO_4$ (with $Co^{2+}$) has not been reported, but exists rather as $Na_5CoO_4$ (with $Co^{3+}$).

In the late 1990s following the early commercial success of the Li-ion battery, these compounds attracted interest as possible positive electrode materials owing to the high Li-content which could provide a very high capacity if realised.[7] Eventually the solid solution series, $Li_{5+x}Fe_{1-x}Co_xO_4$, was tested electrochemically.[8] In more recent times, they have been further investigated as part of an effort to unlock a reversible anionic redox contribution in positive electrode materials to increase the capacity,[9–11] in which the reversible capacity during electrochemical cycling originates not only from oxidation of the transition metal cation, but also partially from the oxygen sublattice. Due to the higher lithium content, they have also attracted interest as pre-lithiation reagents in conventional Li-ion batteries to counter-act the loss of active $Li^+$ during SEI-formation.[12–14] Potential application as $CO_2$-absorbents has also been investigated[15,16] as they readily react with $CO_2$ to form $Li_2CO_3$.

In this work, our focus is the structural and magnetic properties of the solid-solution series $Li_{5+x}Fe_{1-x}Co_xO_4$ ($x = 0.0$, 0.10, 0.18, 0.25, 0.50, 0.60, 0.75 and 1.0). We present structural analysis based on synchrotron X-ray diffraction (XRD), and further report on the high-temperature phase stability of $Li_5FeO_4$, $Li_6CoO_4$ and $Li_{5.50}Fe_{0.50}Co_{0.50}O_4$ up to 900 °C. These results are further elucidated by density functional theory (DFT)

[a] R. V. Thøgersen, A. S. Fjellvåg, H. Fjellvåg
Centre for Materials Science and Nanotechnology, Department of Chemistry, University of Oslo, P.O. Box 1033 Blindern, N-0315 Oslo, Norway
E-mail: helmerf@kjemi.uio.no
[b] Ø. S. Fjellvåg
Department for Hydrogen Technology, Institute for Energy Technology, NO-2027 Kjeller, Norway
[c] Ø. S. Fjellvåg
Laboratory for Neutron Scattering and Imaging, Paul Scherrer Institut, Villigen CH-5232, Switzerland

© 2023 The Authors. Zeitschrift für anorganische und allgemeine Chemie published by Wiley-VCH GmbH. This is an open access article under the terms of the Creative Commons Attribution Non-Commercial License, which permits use, distribution and reproduction in any medium, provided the original work is properly cited and is not used for commercial purposes.

calculations. Furthermore, we have used X-ray absorption near-edge spectroscopy (XANES) to probe the oxidation states of Fe and Co throughout the series, and computed the electronic structures for a subset of the compounds with DFT. Lastly, we present for the first time investigations of the magnetic structures at low temperature (down to 1.5 K) from neutron diffraction of the end-phases, as well as for $Li_{5.50}Fe_{0.50}Co_{0.50}O_4$, accompanied by magnetisation measurements (down to 2 K).

## 2. Results and Discussion

### 2.1. Structural characterisation

The structural properties of the $Li_{5+x}Fe_{1-x}Co_xO_4$-system has been studied based on synchrotron radiation powder diffraction of a selection of intermediate compositions. The two end members take different variants of the antifluorite structure. $Li_5FeO_4$ ($x=0.0$), takes an orthorhombic structure, space group *Pbca* (s.g. 61) with lattice parameters $a=9.225$ Å, $b=9.208$ Å and $c=9.155$ Å.

The second end compound, $Li_6CoO_4$ ($x=1.0$), assumes tetragonal $P4_2/nmc$ (s.g. 137) space group symmetry with lattice parameters $a=b=6.544$ Å and $c=4.651$ Å. The primitive unit cell of $Li_5FeO_4$ can be considered a pseudocubic 2×2×2 supercell of the antifluorite $Li_2O$-structure (s.g. $Fm\bar{3}m$, s.g. 225) (Figure 1a). In $Li_5FeO_4$, one $Li^+$ has been substituted by $Fe^{3+}$ in each of the eight octants, along with the creation of two nearby Li-vacancies in each octant for charge compensation. This phase is denoted the α-phase.[17] For $Li_6CoO_4$, on the other hand, the relation to the same pseudocubic antifluorite supercell is evident after a unit cell transformation that yields new unit cell vectors $\boldsymbol{a}'=\boldsymbol{a}-\boldsymbol{b}$, $\boldsymbol{b}'=\boldsymbol{a}+\boldsymbol{b}$ and $\boldsymbol{c}'=2\boldsymbol{c}$ (Figure 1b). This phase is denoted the β-phase, and differs from the α-phase in the way the transition metal (TM) cations are distributed within the unit cell. In the α-phase, the TM cations are differently positioned in each of the eight octants of the primitive unit cell, while they are more regularly positioned in the β-phase, thus allowing this phase to be described with a smaller unit cell. This positioning of TM cations in the β-phase leads to entire planes consisting of only $Li^+$ within the *ac*- and *bc*-planes of the pseudocubic supercell. There is one less vacancy per TM cation in $Li_6CoO_4$ compared to $Li_5FeO_4$, due to the difference in oxidation state between $Co^{2+}$ and $Fe^{3+}$. However, the β-phase has previously also been reported for compounds with a lower alkali metal ion content, such as $Li_5FeO_4$, $Li_5AlO_4$ and $Na_5InO_4$.[1,18,19] The latter compounds assume an orthorhombic *Pmmn* (s.g. 59) space group symmetry, which is a non-isomorphic subgroup of $P4_2/nmc$, related through an orthorhombic distortion ($a\neq b$) and a splitting of a Li-site (4d) into one fully occupied and one fully vacant site (both 2a). While $Li_6CoO_4$ can be adequately described in the *Pmmn* space group, with an additional lithium in the vacant 2a site, no evidence for any peak splitting was found (Figure S10†), and we conclude that $Li_6CoO_4$ assumes $P4_2/nmc$ space group symmetry at room temperature.

For the solid solution range, the α-phase exists for $x\leq 0.18$, while the β-phase is preferred from $x\geq 0.25$ (Figure 2), indicating a change in phase stability around $0.18<x<0.25$. No clear two-phase situation was detected in any of the samples, although small contributions that could be ascribed to the β- and α-phases, respectively, are observed in $Li_{5.10}Fe_{0.90}Co_{0.10}O_4$ and $Li_{5.25}Fe_{0.75}Co_{0.25}O_4$. In addition, small quantities of unreacted $Li_2O$ are present in all samples (3.0% to 8.9%). Tabulated structural data and Rietveld refinements can be found in Section S1†. The synchrotron powder diffraction data showed tiny peak splittings and shoulders for the intermediate samples

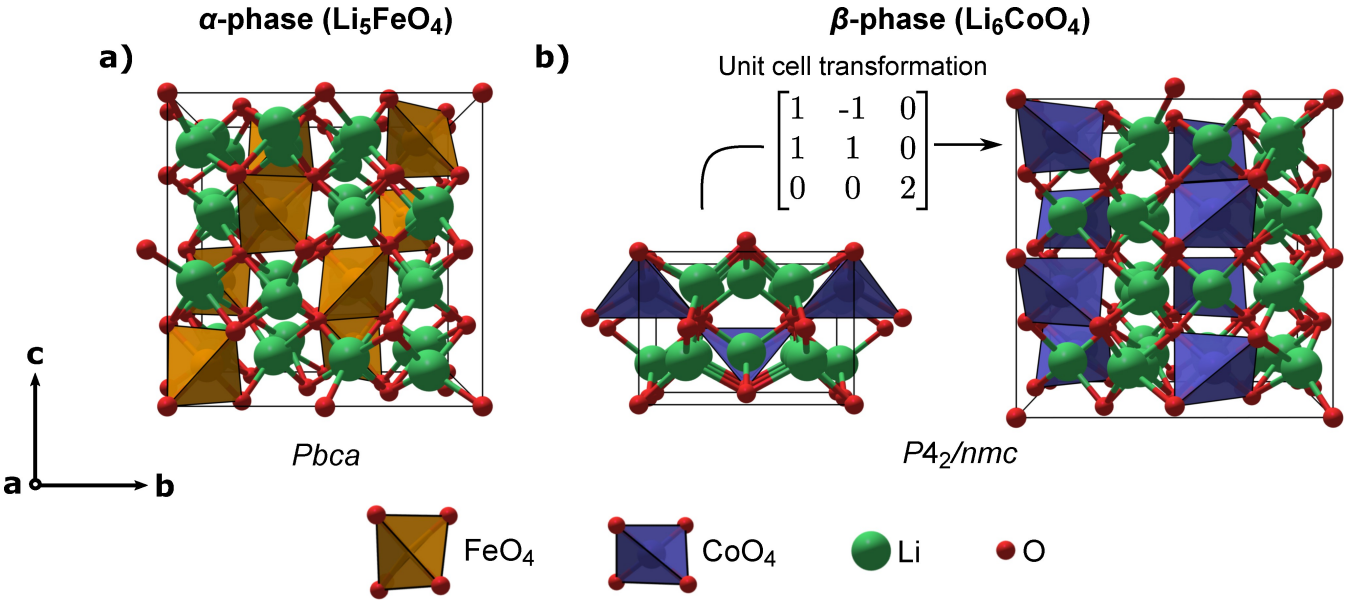


**Figure 1. a)** Primitive unit cell of the α-phase ($Li_5FeO_4$) and **b)** primitive unit cell of the β-phase ($Li_6CoO_4$) along with the unit cell transformation to a 2×2×2 supercell of the antifluorite structure.

 © 2023 The Authors. Zeitschrift für anorganische und allgemeine Chemie published by Wiley-VCH GmbH

15213749, 2023, 22, Downloaded from https://onlinelibrary.wiley.com/doi/10.1002/zaac.202300146 by Norwegian Institute Of Public Healt Invoice Receipt DFO, Wiley Online Library on [31/01/2024]. See the Terms and Conditions (https://onlinelibrary.wiley.com/terms-and-conditions) on Wiley Online Library for rules of use; OA articles are governed by the applicable Creative Commons License

15213749, 2023, 22, Downloaded from https://onlinelibrary.wiley.com/doi/10.1002/zaac.202300146 by Norwegian Institute Of Public Healt Invoice Receipt DFO, Wiley Online Library on [31/01/2024]. See the Terms and Conditions (https://onlinelibrary.wiley.com/terms-and-conditions) on Wiley Online Library for rules of use; OA articles are governed by the applicable Creative Commons License

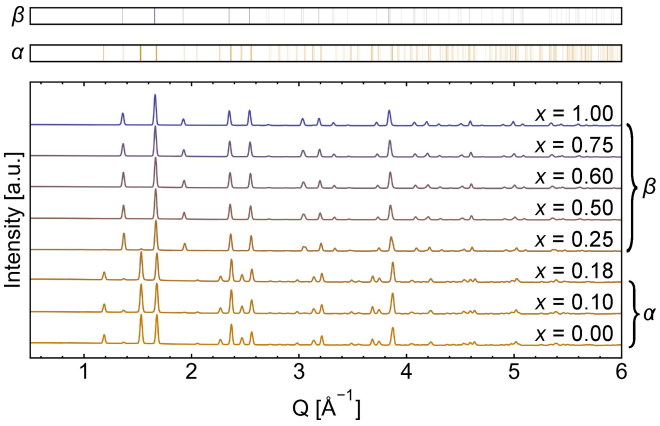


**Figure 2.** Synchrotron X-ray diffractograms of $Li_{5+x}Fe_{1-x}Co_xO_4$ ($\lambda = 0.6888$ Å).

of the β-phase. Hence, these were refined in the *Pmmn* space group, under the assumption that we maintain $Fe^{3+}$ and $Co^{2+}$ throughout the entire series, charge compensated with an additional $Li^+$ in a partially occupied 2a-site. This assumption is substantiated by XANES-analysis in Section 2.3 and magnetic measurements in Section 2.5.

SEM analysis shows a quite broad particle size distribution, with particles ranging from about 5 μm–100 μm. Energy dispersive X-ray elemental mapping analysis (EDS) shows that Fe and Co are well distributed within every particle, with a narrow distribution around the expected (nominal) stoichiometry (Figure 3). Some areas with variations in composition were found, and in e.g. $Li_{5.50}Fe_{0.50}Co_{0.50}O_4$, the largest deviations found from the nominal stoichiometry was ±10% for a small number of particles. No signs of phase segregation were observed, although there is evidence of certain particles devoid of both Fe and Co, in agreement with Rietveld-analysis showing presence of some unreacted $Li_2O$.

The evolution of the lattice parameters and volume of the pseudocubic unit cell, obtained from Rietveld-refinements, show a distinct behaviour for each of the phases (Figure 4). For the α-phase ($x \leq 0.18$), the *a*- and *b*-parameters decrease slightly with increasing *x*, while becoming more similar to each other, while the *c*-parameter increases slightly. This together leads to a small net decrease in volume. From the size differences between $Fe^{3+}$ (0.49 Å, $T_h$ HS) and $Co^{2+}$ (0.58 Å, $T_h$ HS) alone,[20] one would expect a net increase in volume with increasing *x*, although this could be counter-acted by a relaxation of the oxide lattice due to electrostatic effects from additional $Li^+$.

Upon transitioning to the β-phase ($x \geq 0.25$), there is a sharp elongation of the *c*-axis (1.24%), also driving a volume increase. The β-phase follows Vegard's law with a quite linear variation (slight positive departure) in all unit cell parameters with increasing *x*.

A consequence of the applied unit cell transformation of the primitive unit cell of the β-phase to the pseudocubic supercell (Figure 1b), is that the new *a*- and *b*-parameters necessarily become identical. Hence, owing to the tiny peak splittings, we define a normalised orthorhombic distortion parameter $|(a-b)/a|$ (Figure 4, top panel). This parameter will increase with an increasing degree of orthorhombicity, and will equal zero in the tetragonal case. For the β-phase it takes a maximum at $x = 0.5$, before it decreases towards a fully tetragonal cell for $Li_6CoO_4$. These distortions are in all cases quite small, in particular in comparison with e.g. β-$Li_5AlO_4$, where the distortion parameter is 1.85%.[18] For the α-phase, there is a decrease in the corresponding distortion parameter until the phase stability change.

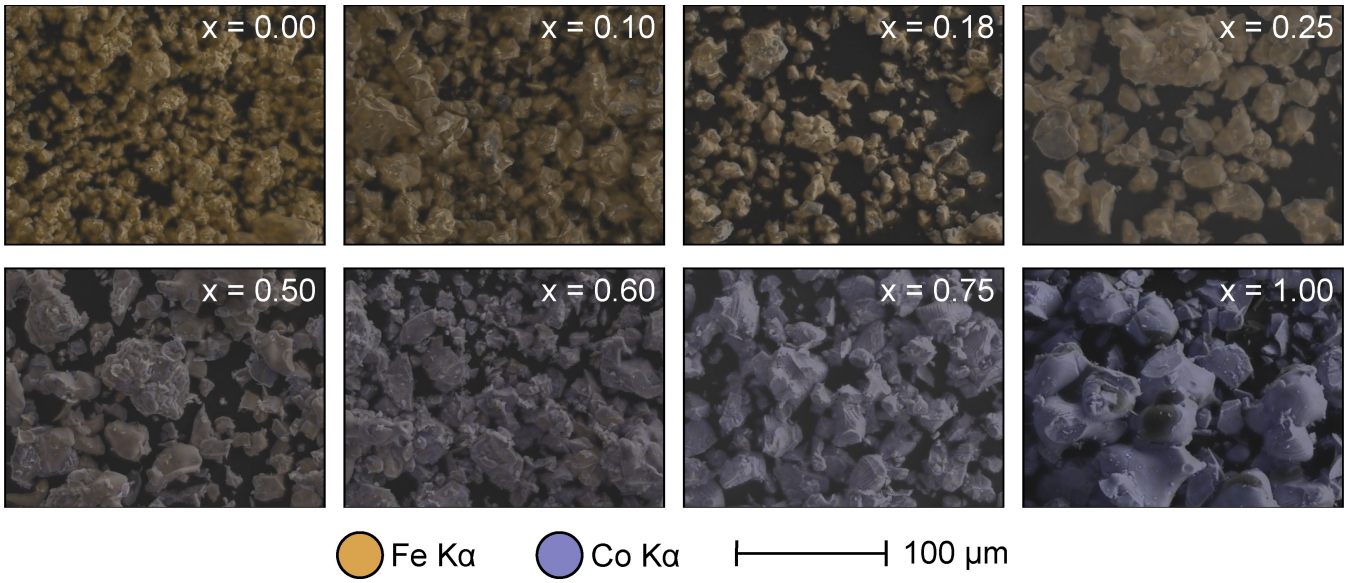


**Figure 3.** EDS-maps of Fe Kα and Co Kα radiation obtained with 17 kV acceleration voltage and a 30 μA beam current overlain on SEM micrographs of $Li_{5+x}Fe_{1-x}Co_xO_4$. The EDS-overlays are weighted according to quantative analysis of the obtained spectra.

 © 2023 The Authors. Zeitschrift für anorganische und allgemeine Chemie published by Wiley-VCH GmbH

15213749, 2023, 22, Downloaded from https://onlinelibrary.wiley.com/doi/10.1002/zaac.202300146 by Norwegian Institute Of Public Healt Invoice Receipt DFO, Wiley Online Library on [31/01/2024]. See the Terms and Conditions (https://onlinelibrary.wiley.com/terms-and-conditions) on Wiley Online Library for rules of use; OA articles are governed by the applicable Creative Commons License

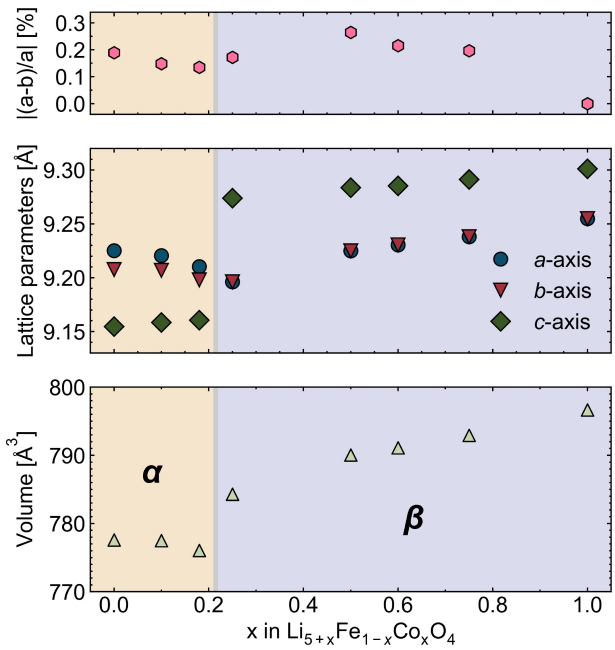


**Figure 4.** Evolution of lattice parameters and volumes of $Li_{5+x}Fe_{1-x}Co_xO_4$ as a function of *x*, based on Rietveld-refinements of synchrotron X-ray diffractograms. The lattice parameters and volumes are reported relative to the 2×2×2- supercell of the antifluorite structure. The lattice parameters of the β-phase (blue area) have been transformed according to the transformation given in Figure 1, meaning that the *a* and *b*- parameters necessarily are equal, with a γ-value departing from 90°. The top panel shows a orthorhombic distortion parameter, $|(a-b)/a|$ of the primitive lattice parameters, to show the degree of orthorhombicity.

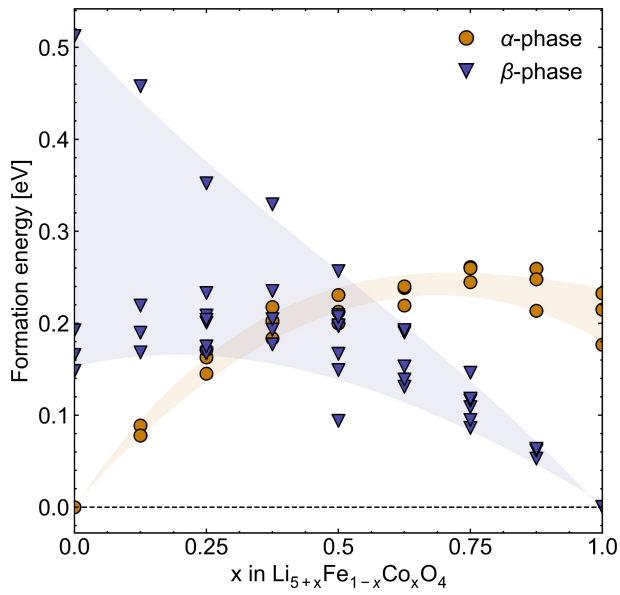


**Figure 5.** The DFT-calculated formation energies of different configurations of the 2×2×2 unit cell of the α-phase vs. the β-phase as a function of *x* in $Li_{5+x}Fe_{1-x}Co_xO_4$. The differences consist of transition metal cation distribution and choice of Li-vacancies. The dashed line shows the convex hull. The shaded areas are only included as visual guides.

To further investigate the relative stability of the β-phase vs. the α-phase, DFT-calculations were performed for intermediate compositions of $Li_{5+x}Fe_{1-x}Co_xO_4$ for the pseudocubic supercell. For each intermediate composition, different configurations of TM cation ordering and different positions of Li-vacancies (of the β-phase) and additional $Li^+$ (of the α-phase) were sampled, and the formation energies with respect to the end-phases were computed (Figure 5). The calculations show a clear stabilisation of the β-phase with increasing *x*, with a crossover at a slightly higher value of *x* ($0.25<x<0.375$) than what is experimentally observed. It is worth noting, that according to just enthalpy considerations, none of the considered phases are stable vs. the end compositions. While entropy of mixing has not been considered here, it is still unlikely that such clear TM cation ordering within the pseudocubic supercell would occur, and we point out that no indications for long-range ordering have been observed experimentally in neither the X-ray diffraction patterns (Figure 2) nor neutron diffraction patterns (Figure 10).

Energy-volume curves were computed for the most stable configurations for $x=0.0$, 0.5 and 1.0 (Figure S27†), and confirm the observed thermodynamic phase stabilities. For $Li_5FeO_4$, the α-phase is favoured by 0.16 eV f.u.$^{-1}$, while for $Li_6CoO_4$ the β-phase is favoured by 0.17 eV f.u.$^{-1}$. For $Li_{5.50}Fe_{0.50}Co_{0.50}O_4$, the difference is smaller, and the β-phase is favoured by only 0.10 eV f.u.$^{-1}$. The γ-structure, which is taken by the Na-analogues,[4,5] was also evaluated and found to be heavily energetically disfavoured, as well as dynamically unstable, as shown from imaginary frequencies in the phonon dispersion relations (Figure S28†).

### 2.2. High- and low-temperature XRD

$Li_5FeO_4$, $Li_{5.50}Fe_{0.50}Co_{0.50}O_4$ and $Li_6CoO_4$ were investigated by high-temperature XRD-measurements. For $Li_5FeO_4$, there is a continuous, close to linear volume thermal expansion until the onset of a phase transition from α (*Pbca*)→β (*Pmmn*) between T=775°C and T=800°C (Figure 6, left panel), consistent with earlier reports.[1] This transition is reconstructive, with relocation of the TM cations in the pseudocubic cell, and is accompanied by a volume increase. This suggests that the β-phase is stabilised at higher volumes, in agreement with the discussion in Section 2.1. This phase transition is also predicted by DFT-calculations, which shows a relative stabilisation of the β-phase vs. the α-phase on increasing temperature (Figure S29†), although the calculations predict the phase change to occur at a higher temperature than what is observed in experiments. While our experiments could not directly determine the reversibility of the phase transition, we conclude that this transition must be reversible as the synthesis temperature is above the transition temperature.

An order-disorder phase transition is identified for $Li_6CoO_4$ at around T=600 °C (Figure 6, right panel). It is manifested as a loss of all but two diffraction peaks (at Q≈2.25 and 3.75 Å$^{-1}$).

 © 2023 The Authors. Zeitschrift für anorganische und allgemeine Chemie published by Wiley-VCH GmbH

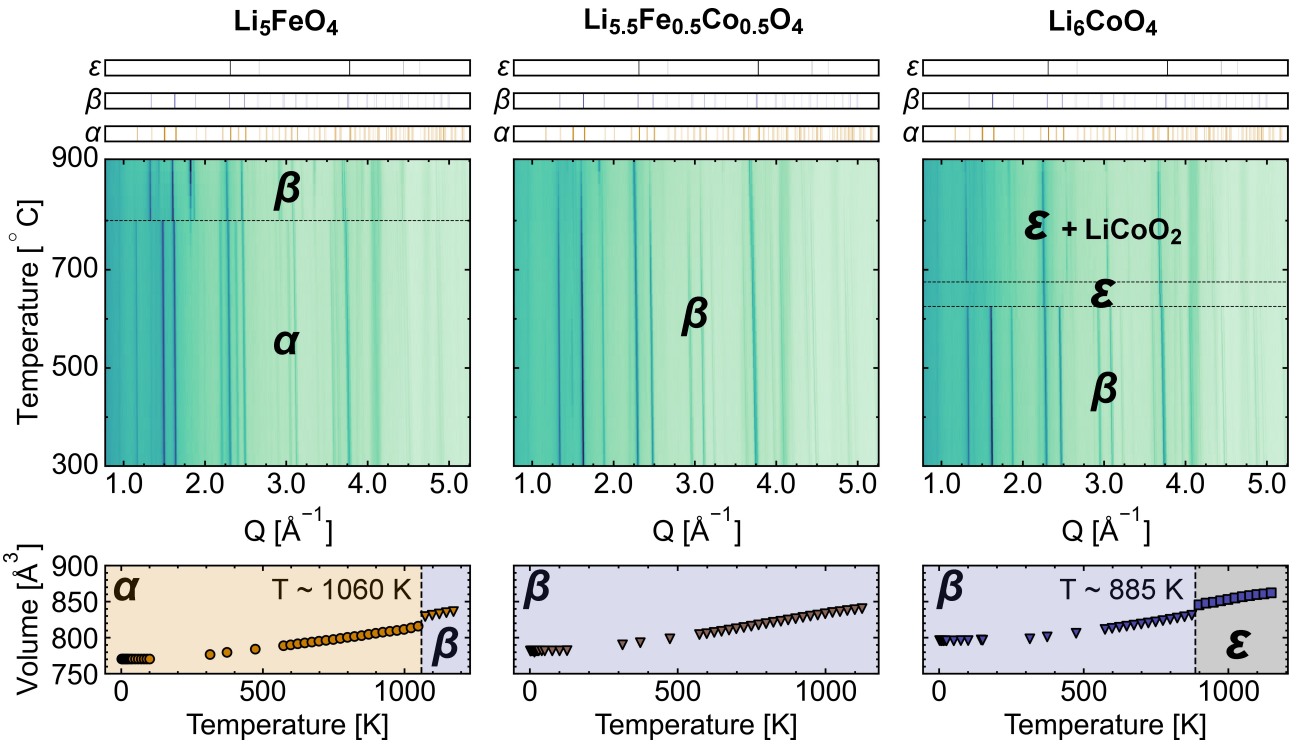


**Figure 6. (Top panels)** X-ray diffractograms as a function of temperature for $Li_5FeO_4$, $Li_{5.50}Fe_{0.50}Co_{0.50}O_4$ and $Li_6CoO_4$ respectively. Scans are 25 °C apart. Dashed lines indicates phase transitions or chemical reactions. **(Bottom panels)** Evolution of unit cell volumes relative to the 2×2×2 antifluorite supercell, obtained from Rietveld refinement. Low temperature data is from neutron diffraction data.

The pattern can be well fitted by assuming a fully cation disordered antifluorite structure ($Fm\bar{3}m$, s.g. 225). We denote the disordered situation as the ε-phase. Such a disordered phase has previously been reported as a result of mechano-chemical treatment of tetragonal $Li_6CoO_4$.[10] This transition is accompanied by a volume increase. At about 50 °C above the phase transition temperature, an oxygen leakage into the capillary triggered oxidation from $Co^{2+}$ to $Co^{3+}$ under the formation of $LiCoO_2$ at the expense of $Li_6CoO_4$. The reaction did not reach completion, and some of the ε-phase persists until 900 °C, allowing refinement up to this temperature. No corresponding phase transition is identified for $Li_{5.50}Fe_{0.50}Co_{0.50}O_4$, and only a steady thermal expansion is observed. Please note that the high Li-content could cause reactions with the quartz capillary under high temperature, however no changes were observed in the diffraction patterns up to the transition temperatures.

Low-temperature synchrotron powder diffraction data of $Li_{5.50}Fe_{0.50}Co_{0.50}O_4$ did not reveal any structural anomalies for temperatures down to 90 K (Figure S9†). This is well in line with the magnetic characterisation data, discussed in Section 2.5. Hence, we suggest that the crystal structure of the β-type phases take space group *Pmmn* for the magnetically ordered state.

### 2.3. Oxidation states

To verify our assumption that we maintain $Fe^{3+}$ and $Co^{2+}$ throughout the series, and that the charge compensation is achieved by the addition of $Li^+$, we performed a series of static X-ray absorption near-edge spectroscopy (XANES) measurements of the Fe and Co K-edges (Figure 7). For all samples, the general spectral shape for both edges is maintained throughout the series. The characteristic main peaks of tetrahedrally coordinated $FeO_4$ and $CoO_4$ (A1-A3) are seen together with the characteristic shoulder (B) and pre-edge feature (C).[21] The main peaks arise from the standard 1s→4p transitions, yielding a final state of $1s1c\ 3d^n\ 4p^1$, where *c* is a core-hole. The shoulder peak B follows from a 1s→4p transition followed by a ligand-to-metal charge transfer, yielding a final state of $1s1c\ 3d^{n+1}\ L4p^1$, where L is a ligand-hole. The intensity of this transition is related to the covalency of the M3*d*-L2*p* bonding, and is expected to be larger in tetrahedral coordination compared to octahedral coordination.[21] Lastly, the pre-edge feature C is due to 1s→3d transitions, which are dipole-forbidden, but quadrupole-allowed ($\triangle l = 2$). However, for a tetrahedrally coordinated transition metal cation, there is a considerable amount of mixing between 3*d*- and 4*p*-orbitals, both of $t_2$-symmetry, whereas in octahedral coordination this mixing is symmetry forbidden ($t_{2g}$ vs. $t_{1u}$).

The centroid position of the C pre-edge feature is very sensitive to oxidation state, an example of which is a shift of about 1.4 eV of the centroid position between $Fe^{2+}$ to $Fe^{3+}$.[22] This variation is used to address whether there is any change in

 © 2023 The Authors. Zeitschrift für anorganische und allgemeine Chemie published by Wiley-VCH GmbH

15213749, 2023, 22, Downloaded from https://onlinelibrary.wiley.com/doi/10.1002/zaac.202300146 by Norwegian Institute Of Public Healt Invoice Receipt DFO, Wiley Online Library on [31/01/2024]. See the Terms and Conditions (https://onlinelibrary.wiley.com/terms-and-conditions) on Wiley Online Library for rules of use; OA articles are governed by the applicable Creative Commons License

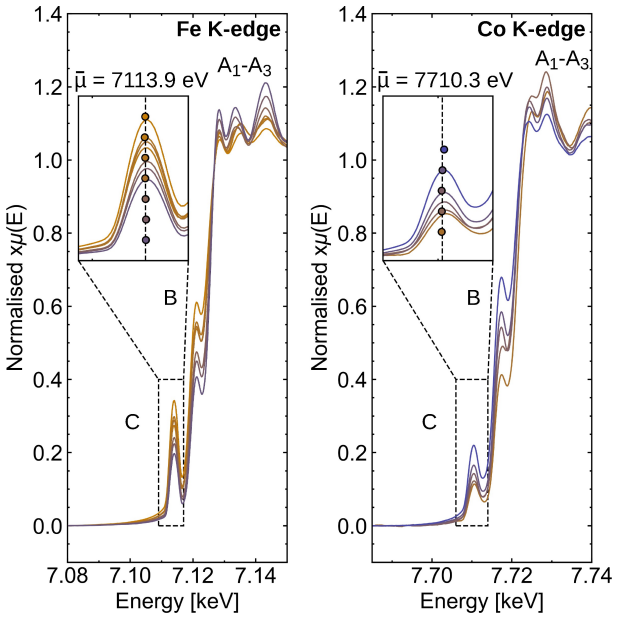


**Figure 7.** XANES of the Fe and Co K-edges. Insets show a zoomed in view of the pre-edge feature, along with the centroid positions of the pre-edge feature. The dashed line shows the mean of the centroid positions, $\bar{\mu}$. For the Co K-edge, spectra for $Li_{5.10}Fe_{0.90}Co_{0.10}O_4$ and $Li_{5.18}Fe_{0.82}Co_{0.18}O_4$ were not obtained.

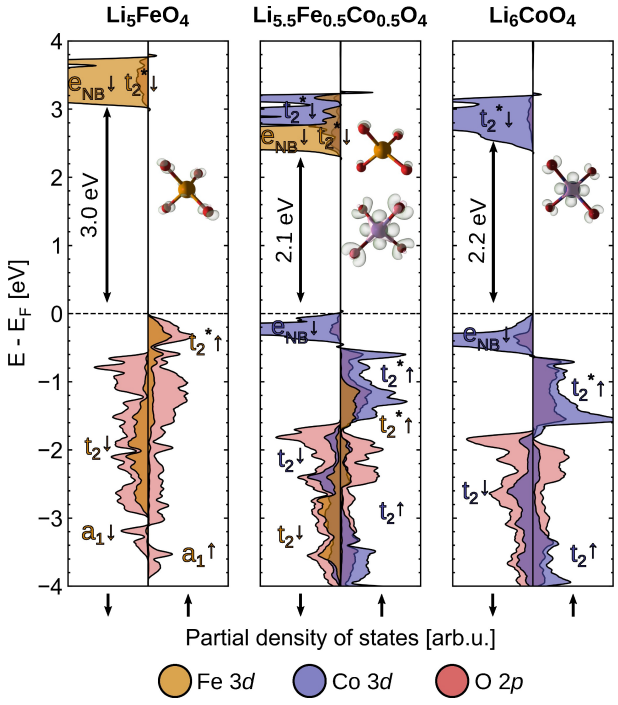


**Figure 8.** DFT-calculated electronic projected densities of states of the Fe 3*d*-, Co 3*d*- and O 2*p*-states for $Li_5FeO_4$, $Li_{5.50}Fe_{0.50}Co_{0.50}O_4$ and $Li_6CoO_4$, respectively. The energies are adjusted to each respective Fermi-level ($E_F$). The insets show the Fukui(−) function around the $FeO_4$- and/or $CoO_4$-tetrahedra. $a_1$-states in $Li_5FeO_4$ also consists of Fe 4*s*-character, not shown here.

oxidation state of Fe and Co throughout the $Li_{5+x}Fe_{1-x}Co_xO_4$-series. The centroid position was obtained by fitting a Pseudo-Voigt function to the peak, and using the fitted value of $\mu$, following a background subtraction (an arctangent function fitted to the data points a few eV below and above the pre-edge peak). All centroid positions are located almost entirely on-top of the mean value, $\bar{\mu} = 7113.9$ eV for the Fe K-edge, and 7710.3 eV for the Co K-edge, with only minor discrepancies (Figure 7, insets), the largest deviation from the mean being 0.06 eV for the Fe K-edge and 0.15 eV for the Co K-edge. This is a clear indication that the oxidation states are constant throughout the series, and that charge compensation for the valence difference comes from additional $Li^+$.

### 2.4. Electronic structures

The electronic density of states, obtained from DFT-calculations, correlates well with what is expected for tetrahedral $d^5$ and $d^7$ high-spin electron configurations, respectively (Figure 8). The highest occupied states in $Li_5FeO_4$ corresponds to Fe 3*d*-orbitals, and from crystal orbital overlap population analysis (Figure S30†), these states are found to be antibonding. This corresponds well with these states being the antibonding $t_2$-orbitals, expected to be the highest occupied orbitals for $Fe^{3+}$. In $Li_6CoO_4$ with $Co^{2+}$ and an additional two *d*-electrons, the highestoccupied states corresponds to the mostly non-bonding *e*- states. The Co 3*d*-states dominate near the Fermi-level ($E_F$) in the inter-mediate $Li_{5.50}Fe_{0.50}Co_{0.50}O_4$, lying above any of the filled Fe-states. There is a large variation in the hybridisation between the TM 3*d*-states and O 2*p*-states near $E_F$. For the Fe–O-states, there is a much larger degree of covalency as seen from a large degree of mixing of Fe- and O-states. This mixing is not so pronounced for the Co–O-states, meaning they exhibit a much more ionic character. Fukui(−) functions were computed to better visualise this (Figure 8, insets). These functions are constructed from the difference in computed charge densities between a pristine system and one in which one electron is removed, revealing the spatial localisation of the highest occupied electrons. These calculations show very O 2*p*-like states for $Li_5FeO_4$, and much purer Co 3*d*-like states for $Li_6CoO_4$ ($d_{x^2-y^2}$). The same Co 3*d*-states dominate at $E_F$ for $Li_{5.50}Fe_{0.50}Co_{0.50}O_4$.

### 2.5. Magnetic properties

Selected samples of $Li_{5+x}Fe_{1-x}Co_xO_4$ ($x = 0.0, 0.18, 0.50, 1.0$) were investigated with respect to magnetic properties at and below room temperature. The two end members, $Li_5FeO_4$ and $Li_6CoO_4$, are briefly described in literature as paramagnetic down to low temperatures.[2,3] $Li_5FeO_4$ is further reported with an antiferro-magnetic transition below 15 K. DC magnetic measurements show that all $Li_{5+x}Fe_{1-x}Co_xO_4$ samples are paramagnetic at elevated temperature (Figure 9). $Li_5FeO_4$ shows the strongest magnetisation in line with the electron configurations of $Fe^{3+}$

 © 2023 The Authors. Zeitschrift für anorganische und allgemeine Chemie published by Wiley-VCH GmbH

15213749, 2023, 22, Downloaded from https://onlinelibrary.wiley.com/doi/10.1002/zaac.202300146 by Norwegian Institute Of Public Healt Invoice Receipt DFO, Wiley Online Library on [31/01/2024]. See the Terms and Conditions (https://onlinelibrary.wiley.com/terms-and-conditions) on Wiley Online Library for rules of use; OA articles are governed by the applicable Creative Commons License

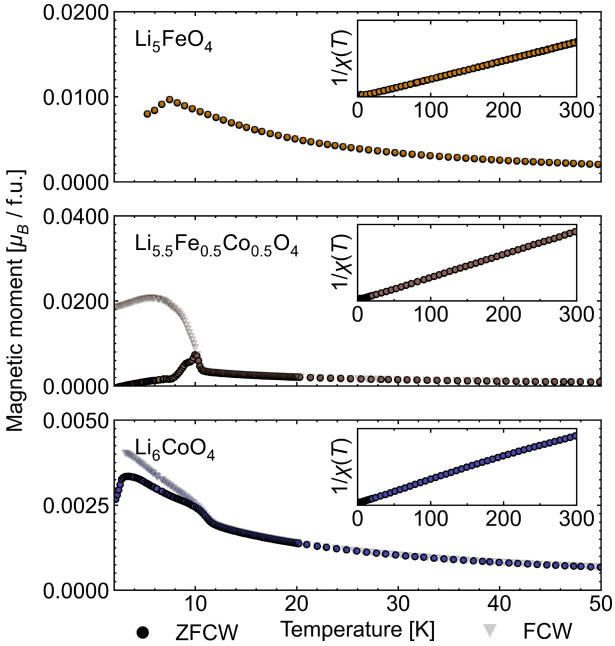


**Figure 9.** DC magnetic measurements of $Li_5FeO_4$, $Li_{5.50}Fe_{0.50}Co_{0.50}O_4$ and $Li_6CoO_4$ measured with a 0.01 T magnetic field. The inset show 1/χ for the same samples measured with a 1 T magnetic field.

and $Co^{2+}$, with 5 and 3 unpaired *d*-electrons, respectively. $Li_5FeO_4$, $Li_{5.18}Fe_{0.82}Co_{0.18}O_4$ (Figure S24†) and $Li_{5.50}Fe_{0.50}Co_{0.50}O_4$ show linear 1/χ-behaviour over a wide temperature range (Figure 9, insets). Their behaviour is close to ideal paramagnetic, and the Curie-Weiss analyses provide Weiss constants (*θ*) close to zero for all three samples (Table 1). The derived effective paramagnetic moments are close to the expected values in the spin only approximation.

$Li_6CoO_4$ deviates from the behaviour of an ideal paramagnet with a slightly non-linear Curie-Weiss region 1/χ (Figure 9, inset bottom panel). The 1/χ behaviour becomes increasingly more linear at higher fields. Curie-Weiss analysis of $Li_6CoO_4$ from 200–300 K measured in a high field (1 T) gives an effective paramagnetic moment of 4.9 $\mu_B$, which is above the expected magnetic moment in the spin only approximation (3*d*-electrons, $\mu_{eff}=3.9\ \mu_B$). For $Co^{2+}$ in tetrahedral coordination, spin orbit coupling can contribute to the magnetic moment, and the observed magnetic moment is in-between the values from the spin-only approximation and the spin orbit coupling value ($\mu_{eff}$ $(J=L+S)=5.7\ \mu_B$) for $L=2$. The close values of the magnetic moment for all samples to theoretical values supports the existence of $Fe^{3+}$ in $Li_5FeO_4$, $Co^{2+}$ in $Li_6CoO_4$ and the coexistence of $Fe^{3+}$ and $Co^{2+}$ for the $Li_{5+x}Fe_{1-x}Co_xO_4$ solid solution.

**Table 1.** Information on the electronic configuration for selected samples in $Li_{5+x}Fe_{1-x}Co_xO_4$, along with the outcome of the analysis of the magnetic measurements and theoretical magnetic moments. For $J=L+S$, $L$ was chosen as 2 for $Li_6CoO_4$.

| | $x=0.0$ | $x=0.18$ | $x=0.50$ | $x=1.0$ |
|---|---|---|---|---|
| Electron configuration | $d^5$ HS | $d^5/d^7$ HS | $d^5/d^7$ HS | $d^7$ HS |
| No. unpaired $e^-$ | 5 | 4.64 | 4 | 3 |
| Temperature (C−W) [K] | 150–350 | 150–300 | 150–300 | 200–300 |
| Weiss constant (*θ*) [K] | 9 | 1 | −3 | −50 |
| $T_N$ [K] | 8 | 12 | 10 | 3 |
| $\mu_{eff}$ (C−W, $H=1$ T) [$\mu_B$] | 6.1 | 5.3[a] | 5.0 | 6.6 |
| $\mu_{eff}$ (spin-only) [$\mu_B$] | 5.9 | 5.55 | 4.9 | 3.9 |
| $\mu_{eff}$ ($J=L+S$) [$\mu_B$] | 5.9 | 5.9[b] | 5.8[b] | 5.7 |
| *M* vs. 1/*H* ($H\rightarrow 0$) [$\mu_B$] | - | 4.6 | 4.4 | - |

[a] ($H=0.5$ T) [b] $\sqrt{(xm_{Li_6CoO_4}).2\ +\ ((1-x)m_{Li_5FeO_4}).2}$

Field dependent magnetisation data show that both of the solid solution samples ($x=0.18$ and 0.50) are easily magnetised at low temperature, and $x=0.18$ is approaching a saturation at 9 T (Figure S25†). By plotting *M* vs. 1/*H*, a saturation magnetisation is extracted, which is close to the average number of unpaired electrons in the two samples (Table 1). Additionally, $x=0.18$ shows a metamagnetic transition at 4 K as a function of magnetic field strength, at around 5 T. The origin of the transition remains unknown and is recommended for further studies.

At low temperatures, magnetic transitions occur for all measured samples in the range of 3 K to 12 K (Table 1). For $Li_5FeO_4$, there is a reduction in both the zero-field cooled (ZFC) and field-cooled (FC) magnetisations at just below 8 K (Figure 9, top panel), indicating an antiferromagnetic transition, in agreement with previous reports by Luge and Hoppe.[2] For $Li_6CoO_4$, the *M*(*T*)-data shows first a clear increase at temperatures below 12 K, followed by a sharp decrease below 3 K (Figure 9, bottom panel). Since the powder neutron diffraction data (discussed below) show additional magnetic peaks at 1.5 K that have disappeared already at 5 K, we interpret this first increase to reflect short range magnetic interactions. The dip in the magnetisation at around 3 K is hence likely to correspond to the onset of long-range magnetic ordering. The low intensity of the magnetisation (and negative Weiss constant of −50 K) indicates dominating antiferromagnetism. For the solid solution samples with composition $x=0.18$ (Figure S24†) and 0.50 (Figure 9, middle panel), the ZFC data indicate several small consecutive transitions between 7 K to 12 K. Below the transition temperature, the ZFC and FC data differ significantly, indicating that the transition is not of pure antiferromagnetic nature, and the FC data suggests a small ferromagnetic component below $T_N$. However, the magnetisation intensity is low and the samples are likely dominated by antiferromagnetic interactions. This may be linked to the coexistence of $Fe^{3+}$ and $Co^{2+}$, causing additional interactions compared to the end members. AC magnetic measurements of the $x=0.18$ sample show that magnetic interactions start already at 30 K, identified by intensity in the imaginary component of the AC magnetisation (Figure S26†, bottom left panel). Intensity from the 2nd and 3rd harmonic further confirm that a magnetic transition occur at 8 K that is not of pure antiferromagnetic nature (Figure S26†, top panels).

The long-range magnetic structures for $Li_5FeO_4$, $Li_{5.50}Fe_{0.50}Co_{0.50}O_4$ and $Li_6CoO_4$ were investigated by powder

 © 2023 The Authors. Zeitschrift für anorganische und allgemeine Chemie published by Wiley-VCH GmbH

15213749, 2023, 22, Downloaded from https://onlinelibrary.wiley.com/doi/10.1002/zaac.202300146 by Norwegian Institute Of Public Healt Invoice Receipt DFO, Wiley Online Library on [31/01/2024]. See the Terms and Conditions (https://onlinelibrary.wiley.com/terms-and-conditions) on Wiley Online Library for rules of use; OA articles are governed by the applicable Creative Commons License

15213749, 2023, 22, Downloaded from https://onlinelibrary.wiley.com/doi/10.1002/zaac.202300146 by Norwegian Institute Of Public Healt Invoice Receipt DFO, Wiley Online Library on [31/01/2024]. See the Terms and Conditions (https://onlinelibrary.wiley.com/terms-and-conditions) on Wiley Online Library for rules of use; OA articles are governed by the applicable Creative Commons License

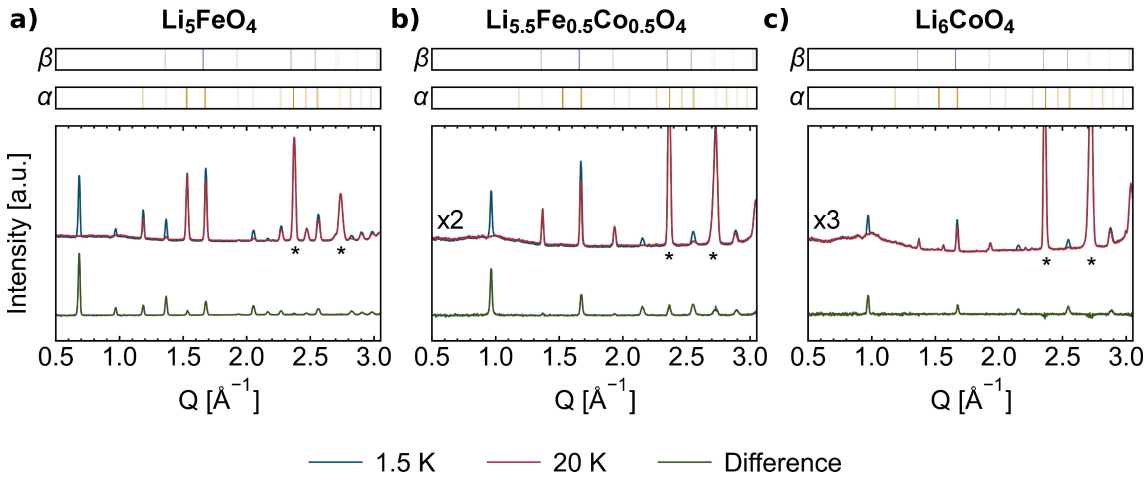


**Figure 10.** Neutron diffractograms at below (1.5 K) and above (20 K) the magnetic ordering temperatures for **a)** $Li_5FeO_4$, **b)** $Li_{5.50}Fe_{0.50}Co_{0.50}O_4$ and **c)** $Li_6CoO_4$, respectively. The difference is shown underneath, showing only contributions from the magnetic structure. The diffractogram of $Li_{5.50}Fe_{0.50}Co_{0.50}O_4$ is multiplied by a factor of 2, and of $Li_6CoO_4$ by a factor of 3, to compensate for the lower neutron scattering length of Co compared to Fe. The peaks marked by asterisks have large contributions from the Al-sample holder.

neutron diffraction at 1.5 K (Figure 10). Clear magnetic ordering peaks are visible for all three samples at 1.5 K, and disappear on heating at 7.5 K for $Li_5FeO_4$ and $Li_{5.50}Fe_{0.50}Co_{0.50}O_4$, and already at 5 K for $Li_6CoO_4$. For $Li_5FeO_4$ and $Li_6CoO_4$, this is in good agreement with the measurements discussed above, however the *M*(*T*)-data (ZFC and FC) for $Li_{5.50}Fe_{0.50}Co_{0.50}O_4$ suggests a somewhat higher ordering temperature of 10 K.

The $Li_6CoO_4$ and $Li_{5.50}Fe_{0.50}Co_{0.50}O_4$ samples show very similar magnetic Bragg scattering with weak magnetic Bragg peaks, while $Li_5FeO_4$ shows significantly stronger magnetic Bragg peaks. The strength of the magnetic Bragg scattering is indicating the magnitude of the ordered magnetic moment, and it is clear that the ordered magnetic moment decreases with $x$ in $Li_{5+x}Fe_{1-x}Co_xO_4$.

We started the evaluation of magnetic structures with $Li_5FeO_4$ by representation analysis in the Jana2020 software.[23] The magnetic structure of $Li_5FeO_4$ is indexed by $k=(0, 0, 0)$. Careful evaluation of all the possible magnetic space groups indicates that the compound is best described in *Pbc′a* with the moment along [001] (Figure 11). In the Rietveld refinements, the $M_x$ and $M_y$ moments were restricted to zero as they had a minor impact on the refinement. In *Pbc′a*, the Fe–Fe pair with the shortest distance is coupled antiferromagnetically while the pair with the second shortest distance is ferromagnetically coupled. In the *ab*-plane, the moments are thus antiferromagnetically coupled. The refined magnetic moment for Fe at 1.5 K is 3.65(3) $\mu_B$, which is lower than the expected value of 5 $\mu_B$ for $Fe^{3+}$.

$Li_6CoO_4$ and $Li_{5.50}Fe_{0.50}Co_{0.50}O_4$ are close to being indexed by $k=(0, 0, 0)$. However, Le Bail-refinements clearly show that the magnetic peak at 2.2 $Å^{-1}$ is shifted away from $k=(0, 0, 0)$. The nuclear structure is well described at 20 K in the tetragonal and orthorhombic unit cells, respectively, so a structural distortion is not the origin of this shift, well in line with results from low-temperature XRD of $Li_{5.50}Fe_{0.50}Co_{0.50}O_4$ (Section 2.2). We thus

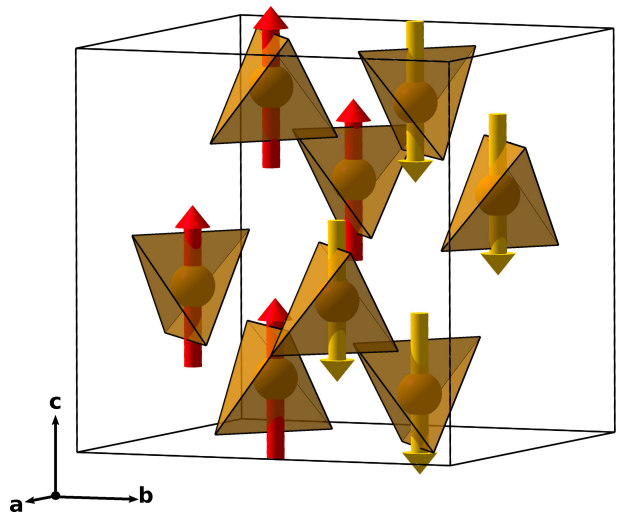


**Figure 11.** The refined magnetic structure of $Li_5FeO_4$. The refinement was done in the *Pbc′a* magnetic space group, where the $M_x$ and $M_y$ moments were restricted to zero.

conclude that the propagation vector is incommensurate. With the limited number of magnetic Bragg peaks, we could not unambiguously index the magnetic structure and thus not describe it in detail. We note that Rietveld refinements with a commensurate model describe the data decently but with clear discrepancies, e.g. the 2.2 $Å^{-1}$ peak position. In these refinements, we reduced the symmetry to $P2_1/m'$ and used $M_x$ and $M_z$ components for the magnetic site (Figures S12 and S13†).

## 3. Conclusions

We have synthesised and characterised several compounds in the $Li_{5+x}Fe_{1-x}Co_xO_4$-series ($x=0.0$, 0.10, 0.18, 0.25, 0.50, 0.60,

 © 2023 The Authors. Zeitschrift für anorganische und allgemeine Chemie published by Wiley-VCH GmbH

15213749, 2023, 22, Downloaded from https://onlinelibrary.wiley.com/doi/10.1002/zaac.202300146 by Norwegian Institute Of Public Healt Invoice Receipt DFO, Wiley Online Library on [31/01/2024]. See the Terms and Conditions (https://onlinelibrary.wiley.com/terms-and-conditions) on Wiley Online Library for rules of use; OA articles are governed by the applicable Creative Commons License

0.75 and 1.0). The end members, $Li_5FeO_4$ and $Li_6CoO_4$, assume an orthorhombic (*Pbca*) and tetragonal ($P4_2/nmc$) crystal structure, respectively, denoted the α- and β-phases. The intermediate compounds form as the α-phase until a change in preference for the β-phase occurs somewhere in the interval $0.18 < x < 0.25$. We show that the same change in phase occurs for $Li_5FeO_4$ at elevated temperatures (~1060 K), while $Li_6CoO_4$ show an order-disorder transition into a fully cation-disordered structure (~885 K), denoted the ε-phase. For all members of the series, the transition metals remain in their $Fe^{3+}$ and $Co^{2+}$ oxidation states, where charge compensation with increasing *x* happens through additional $Li^+$. Electronic structure calculations show a higher degree of covalency for bonding in the $FeO_4$-tetrahedra compared to the $CoO_4$-tetrahedra. Neutron diffraction shows that long-range magnetic ordering is present in $Li_5FeO_4$, $Li_{5.50}Fe_{0.50}Co_{0.50}O_4$, and $Li_6CoO_4$ at low temperatures. The antiferromagnetic structure of $Li_5FeO_4$ is described in the magnetic space group *Pbc′a*, while the magnetic structures of $Li_{5.50}Fe_{0.50}Co_{0.50}O_4$ and $Li_6CoO_4$ are slightly incommensurate.

## Experimental Section

**Materials synthesis** Powder samples of $Li_{5+x}Fe_{1-x}Co_xO_4$ ($x = 0.0$, 0.10, 0.18, 0.25, 0.50, 0.60, 0.75, 1.0) were synthesised from stoichiometric mixtures of $Li_2O$ (Sigma-Aldrich, 97 %):$Fe_2O_3$ (Acros Organics, 99.999 % trace metal basis):CoO (Acros Organics, > 99 %) through a solid-state reaction pathway. As $Li_2O$ readily reacts with moisture in the atmosphere to form LiOH, the reactant powder was first subjected to heat treatment at 500 °C for 12 h under an Ar-flow of 100 ml/min in a semiclosed system to decompose and remove LiOH prior to mixing. Since both $Li_2O$ and $Li_{5+x}Fe_{1-x}Co_xO_4$ reacts with moisture and $CO_2$ in ambient air, all processing steps were done in an Ar-filled glovebox. The precursors were manually ground for 20 minutes. The solid state reactions were done in a split furnace where the mixed precursors were placed in an alumina boat inside a quartz tube capped at both ends with adaptors to keep the system closed. These adaptors could then be connected to either an Ar-flow or a vacuum pump, and at the end of the synthesis transferred back to the glovebox for further handling. $Li_5FeO_4$ was synthesised in a semi-closed setup under an Ar-flow of 100 ml/min for 20 h, while all other compositions were synthesised in a closed setup under vacuum in order to prevent any oxidation of $Co^{2+}$ to $Co^{3+}$ from trace amounts of oxygen in the Ar-gas. A summary of the synthesis conditions is given in Table S10 (ESI†). All products were further hand-ground in an agate mortar prior to subsequent experiments.

**X-ray diffraction (XRD)** Synchrotron radiation powder X-ray diffraction data for Rietveld refinement of lattice parameters and atomic positions were collected at the Swiss-Norwegian Beamlines (SNBL, BM01), ESRF, Grenoble with a Pilatus2 M 2D detector and a wavelength of 0.6888 Å. The samples were contained in 0.5 mm borosilicate capillaries that were rotated 90° during the 10 s exposure. The data was collected at a detector distance of 139.2 mm from the sample. The 2D-data was integrated using the azimuthal integrator implemented in pyFAI,[24] and the measurements were calibrated with $LaB_6$ (NIST Standard Reference Material 660c). Pixel corrections were done to correct for inaccuracies in experimental geometry according to the method outlined by Wright et al.[25] The peak shape was fitted to the aforementioned $LaB_6$ standard with the resolution function for area detectors by Chernyshov et al.[26] High-temperature powder XRD measurements for samples contained in 0.7 mm quartz capillaries were carried out in the RECX homelab using a Bruker D8 difractometer, an Anton Paar HTK-1200 N heating chamber and Mo Kα-radiation. The heating chamber was calibrated from refinement of diffraction data from a silver standard. As diffractograms obtained by various radiation sources are presented, all patterns are given in *Q*, with the relation to the wavelength of the radiation (λ) and the scattering angle (θ) given by $Q = \frac{4\pi}{\lambda} \sin\theta$ . All refinements were done in TOPAS V6.[27]

**X-ray absorption near-edge spectroscopy (XANES)** The XANES-data was measured in fluorescence mode at SNBL, BM31. Spectra of Fe- and Co-metal foils were captured before sample measurements, and were used to calibrate the energy against tabulated values in International Tables for Crystallography Vol. C.[28] Linear functions were fitted to the pre-edge and post-edge areas, where the pre-edge function was subtracted from the data. Each spectrum was later normalised by dividing by the difference between the pre-edge and post-edge fitted functions at the edge position. The centroid position of pre-edge features was determined by fitting a Pseudo-Voigt peak function to the feature following a subtraction of a background fitted to an arctangent function. All curve fits were done using a non-linear least squares method as implemented in SciPy.[29]

**Neutron diffraction (ND)** Powder neutron diffraction data were collected at the DMC instrument at the continuous spallation source SINQ, PSI, Switzerland at a wavelength of 3.812 Å. The samples were cooled in ILL5, a 100 mm Orange He cryostat. Diffraction patterns were collected on powder samples in Al cans at 1.5, 2.5, 5.0, 7.5, 10.0, 12.5, 15.0, 17.5, 20.0, 25.0, 30.0, 35.0, 40.0, 50.0, 75.0 and 100.0 K, and analysed using Jana2020[23] and TOPAS V6.[27]

**Magnetic measurements** Magnetic measurements were performed using a Quantum Design physical properties measurement system (QD-PPMS). The samples were measured during heating from 2 to 300 K using a 100 and 10000 Oe external DC-field, first after an initial cooling without applied field (zero-field cooled, ZFC), then after a second cooling with applied field (field cooled, FC). Hysteresis measurements were carried out for $Li_{5.18}Fe_{0.82}Co_{0.18}O_4$ ($-9 < H < 9$ T) and $Li_{5.50}Fe_{0.50}Co_{0.50}O_4$ ($-6 < H < 6$ T).

**Scanning electron microscopy (SEM) & Energy dispersive X-ray spectroscopy (EDS)** SEM-micrographs were obtained using a Hitachi SU8230 scanning electron microscope at an acceleration voltage ($V_{acc}$) of 1 kV and a beam current of 5 μA for $x \leq 0.5$ and 10 μA for $x > 0.5$. EDS-spectra were obtained using a Bruker XFlash 6-10 X-ray detector with $V_{acc} = 17$ kV and a beam current of 30 μA.

**Density functional theory (DFT)** DFT-calculations were performed using the projected-augmented-wave (PAW)[30,31] implementation of the Vienna Ab initio Simulation Package (VASP 5.4.4).[32–35] The Perdew, Burke and Ernzerhof (PBE) functional[36] is used for the exchange-correlation term using an energy cutoff of 520 eV. The Hubbard parameter U is used following the rotationally invariant form by Dudarev and Botton.[37] The effective U-value for the *d*-orbitals is set to 5.3 eV for Fe and 3.32 eV for Co in correspondance with calibrated values for oxide systems by the Materials Project, which were obtained by fitting to experimental binary formation enthalpies.[38] The optimised structures are obtained by minimising the total energy with a convergence criterion of $10^{-4}$ eV using the conjugate gradient algorithm. The convergence threshold for the electronic self-consistent calculations are set to $10^{-6}$ eV. Brillouin zone (BZ) integration is performed with a Γ-centered grid with a smallest allowed spacing between *k*-points of 0.4 $Å^{-1}$. The BZ integration is done using Guassian smearing with broadening width of 0.2 eV. Energy-volume curves are fitted to the Birch-Murnaghan

 © 2023 The Authors. Zeitschrift für anorganische und allgemeine Chemie published by Wiley-VCH GmbH

15213749, 2023, 22, Downloaded from https://onlinelibrary.wiley.com/doi/10.1002/zaac.202300146 by Norwegian Institute Of Public Healt Invoice Receipt DFO, Wiley Online Library on [31/01/2024]. See the Terms and Conditions (https://onlinelibrary.wiley.com/terms-and-conditions) on Wiley Online Library for rules of use; OA articles are governed by the applicable Creative Commons License

equation of state[39] to obtain equilibrium values for the total energy, volume, bulk modulus and its pressure derivative. The phonopy package was used to construct displacements for all phonon calculations.[40] For these calculations, we construct supercells when needed to ensure that each lattice parameter is at least 9 Å. First, we allow the structure to relax using a stricter convergence criterion with a force convergence threshold of 10 meV $Å^{-1}$ and electronic convergence criterion of $10^{-8}$ eV. The forces are then calculated for all displacements using the same electronic convergence criterion where all projection operators are evaluated in reciprocal space for added accuracy, as opposed to the automatic scheme provided by VASP used in all other calculations. We employ the finite differences method with displacements lengths of 0.1 Å. The phonopy package is further used to calculate the phonon dispersion relations, and the thermal properties used to extrapolate phase stability with increasing temperature. The convex hull is constructued as outlined by Urban et al.[41] from

$$\Delta E_{form}(1-x) = E(1-x) - (1-x)E(1) - xE(0)$$

where the E(1) and E(0) are the total energies of the end compositions $Li_6CoO_4$ and $Li_5FeO_4$ and $E(1-x)$ $(0 \leq x \leq 1)$ is the total energy of an intermediate composition a distance $x$ from E(0) and $(1-x)$ from E(1), from which $E_{form}(0)$ and $E_{form}(1)$ are set to 0 by construction.

## Acknowledgements

The authors gratefully express thanks for being granted synchrotron beamtime at SNBL (ESRF) and NcNeutron (NFR project 245942) in collaboration with PSI for neutron beamtime at SINQ, as well for skilful assistance, and in particular Hermann Emerich (SNBL) for XANES-measurements during remote beamtime. ØSF acknowledges funding from NFR (project 325345). We further acknowledge the use of the Norwegian national infrastructure for X-ray diffraction and Scattering (RECX) and the Research Council of Norway for providing the computer time (under the project numbers NN2875k and NS2875k) at the Norwegian supercomputer facility. Lastly, we acknowledge Martin Valldor (UiO), Yohann Breard (CRISMAT, Caen) and Fabien Veillon (CRISMAT, Caen) for their help and expertise in performing low temperature magnetic measurements, and the assistance from Walace Kierulf-Vieira (UiO) in SEM and EDS data acquisition.

## Conflict of Interest

The authors report no conflicts of interest.

## Data Availability Statement

The data that support the findings of this study are available from the corresponding author upon reasonable request.

**Keywords:** Oxides · X-ray diffraction · X-ray absorption spectroscopy · Neutron diffraction · Magnetic properties

[1] G. Demoisson, F. Jeannot, C. Gleitzer, J. Aubry, *C. R. Acad. Sc. Paris* **1971**, *272*, 458–461.
[2] R. Luge, R. Hoppe, *ZAAC - J. Inorg. Gen. Chem.* **1984**, *513*, 141–150.
[3] R. Luge, R. Hoppe, *ZAAC - J. Inorg. Gen. Chem.* **1986**, *534*, 61–68.
[4] G. Brachtel, R. Hoppe, *ZAAC - J. Inorg. Gen. Chem.* **1978**, *446*, 77–86.
[5] W. Burow, R. Hoppe, *Naturwissenschaften* **1980**, *67*, 192.
[6] R. V. Thøgersen, F. Bianchini, H. Fjellvåg, P. Vajeeston, *RSC Adv.* **2022**, *12*, 17410–17421.
[7] S. Narukawa, Y. Takeda, M. Nishijima, N. Imanishi, O. Yamamoto, M. Tabuchi, *Solid State Ionics* **1999**, *122*, 59–64.
[8] N. Imanishi, Y. Inoue, A. Hirano, M. Ueda, Y. Takeda, H. Sakaebe, M. Tabuchi, *J. Power Sources* **2005**, *146*, 21–26.
[9] C. Zhan, Z. Yao, J. Lu, L. Ma, V. A. Maroni, L. Li, E. Lee, E. E. Alp, T. Wu, J. Wen, Y. Ren, C. Johnson, M. M. Thackeray, M. K. Chan, C. Wolverton, K. Amine, *Nat. Energy* **2017**, *2*, 963–971.
[10] H. Kobayashi, T. Tsukasaki, Y. Ogasawara, M. Hibino, T. Kudo, N. Mizuno, I. Honma, K. Yamaguchi, *ACS Appl. Mater. Interfaces* **2020**, *12*, 43605–43613.
[11] Z. Yao, M. K. Chan, C. Wolverton, *Chem. Mater.* **2022**, *34*, 4536–4547.
[12] C. S. Johnson, S. H. Kang, J. T. Vaughey, S. V. Pol, M. Balasubramanian, M. M. Thackeray, *Chem. Mater.* **2010**, *22*, 1263–1270.
[13] X. Su, C. Lin, X. Wang, V. A. Maroni, Y. Ren, C. S. Johnson, W. Lu, *J. Power Sources* **2016**, *324*, 150–157.
[14] J. Li, B. Zhu, S. Li, D. Wang, W. Zhang, Y. Xie, J. Fang, B. Hong, Y. Lai, Z. Zhang, *J. Electrochem. Soc.* **2021**, *168*, 080510.
[15] H. A. Lara-García, P. Sanchez-Camacho, Y. Duan, J. Ortiz-Landeros, H. Pfeiffer, *J. Phys. Chem. C* **2017**, *121*, 3455–3462.
[16] H. A. Lara-García, E. Vera, J. A. Mendoza-Nieto, J. F. Gómez-García, Y. Duan, H. Pfeiffer, *Chem. Eng. J.* **2017**, *327*, 783–791.
[17] F. Stewner, R. Hoppe, *Acta Crystallogr. Sect. B* **1971**, *27*, 616–621.
[18] R. Hoppe, H. König, *ZAAC - J. Inorg. Gen. Chem.* **1977**, *430*, 211–217.
[19] H. Glaum, R. Hoppe, *ZAAC - J. Inorg. Gen. Chem.* **1990**, *583*, 24–30.
[20] R. D. Shannon, *Acta Crystallogr. Sect. A* **1976**, *32*, 751–767.
[21] T. Okumura, M. Shikano, H. Kobayashi, *J. Mater. Chem. A* **2014**, *2*, 11847–11856.
[22] M. Wilke, F. Farges, P. E. Petit, G. E. Brown, F. Martin, *Am. Mineral.* **2001**, *86*, 714–730.
[23] V. Petříček, L. Palatinus, J. Plášil, M. Dušek, *Z. Für Krist. - Cryst. Mater.* **2023**, *0*, 1–12.
[24] J. Kieffer, V. Valls, N. Blanc, C. Hennig, *J. Synchrotron Radiat.* **2020**, *27*, 558–566.
[25] J. P. Wright, C. Giacobbe, E. L. Bright, *Crystals* **2022**, *12*, 1–8.
[26] D. Chernyshov, V. Dyadkin, H. Emerich, G. Valkovskiy, C. J. McMonagle, W. van Beek, *Acta Crystallogr. Sect. Found. Adv.* **2021**, *77*, 497–505.
[27] A. A. Coelho, *J. Appl. Crystallogr.* **2018**, *51*, 210–218.
[28] *International Tables for Crystallography, Volume C* (Ed.: A. J. C. Wilson), Kluwer Academic Publishers, Dordrecht/Boston/London, **1992**.
[29] P. Virtanen, R. Gommers, T. E. Oliphant, M. Haberland, T. Reddy, D. Cournapeau, E. Burovski, P. Peterson, W. Weckesser, J. Bright, S. J. van der Walt, M. Brett, J. Wilson, K. J. Millman, N. Mayorov, A. R. Nelson, E. Jones, R. Kern, E. Larson, C. J. Carey, İ. Polat, Y. Feng, E. W. Moore, J. VanderPlas, D. Laxalde, J.

 © 2023 The Authors. Zeitschrift für anorganische und allgemeine Chemie published by Wiley-VCH GmbH

Perktold, R. Cimrman, I. Henriksen, E. A. Quintero, C. R. Harris, A. M. Archibald, A. H. Ribeiro, F. Pedregosa, P. van Mulbregt, A. Vijaykumar, A. P. Bardelli, A. Rothberg, A. Hilboll, A. Kloeckner, A. Scopatz, A. Lee, A. Rokem, C. N. Woods, C. Fulton, C. Masson, C. Häggström, C. Fitzgerald, D. A. Nicholson, D. R. Hagen, D. V. Pasechnik, E. Olivetti, E. Martin, E. Wieser, F. Silva, F. Lenders, F. Wilhelm, G. Young, G. A. Price, G. L. Ingold, G. E. Allen, G. R. Lee, H. Audren, I. Probst, J. P. Dietrich, J. Silterra, J. T. Webber, J. Slavič, J. Nothman, J. Buchner, J. Kulick, J. L. Schönberger, J. V. de Miranda Cardoso, J. Reimer, J. Harrington, J. L. C. Rodríguez, J. Nunez-Iglesias, J. Kuczynski, K. Tritz, M. Thoma, M. Newville, M. Kümmerer, M. Bolingbroke, M. Tartre, M. Pak, N. J. Smith, N. Nowaczyk, N. Shebanov, O. Pavlyk, P. A. Brodtkorb, P. Lee, R. T. McGibbon, R. Feldbauer, S. Lewis, S. Tygier, S. Sievert, S. Vigna, S. Peterson, S. More, T. Pudlik, T. Oshima, T. J. Pingel, T. P. Robitaille, T. Spura, T. R. Jones, T. Cera, T. Leslie, T. Zito, T. Krauss, U. Upadhyay, Y. O. Halchenko, Y. Vázquez-Baeza, *Nat. Methods* **2020**, *17*, 261–272.

[30] P. E. Blöchl, *Phys. Rev. B* **1994**, *50*, 17953–17979.

[31] G. Kresse, D. Joubert, *Phys. Rev. B* **1999**, *59*, 1758–1775.

[32] G. Kresse, J. Hafner, *Phys. Rev. B* **1993**, *47*, 558–561.

[33] G. Kresse, J. Hafner, *Phys. Rev. B* **1994**, *49*, 14251–14269.

[34] G. Kresse, J. Furthmüller, *Comput. Mater. Sci.* **1996**, *6*, 15–50.

[35] G. Kresse, J. Furthmüller, *Phys. Rev. B* **1996**, *54*, 11169–11186.

[36] J. P. Perdew, K. Burke, M. Ernzerhof, *Phys. Rev. Lett.* **1996**, *77*, 3865–3868.

[37] S. Dudarev, G. Botton, *Phys. Rev. B* **1998**, *57*, 1505–1509.

[38] A. Jain, S. P. Ong, G. Hautier, W. Chen, W. D. Richards, S. Dacek, S. Cholia, D. Gunter, D. Skinner, G. Ceder, K. A. Persson, *APL Mater.* **2013**, *1*, 011002.

[39] M. Hebbache, M. Zemzemi, *Phys. Rev. B* **2004**, *70*, 5–10.

[40] A. Togo, I. Tanaka, *Scr. Mater.* **2015**, *108*, 1–5.

[41] A. Urban, D. H. Seo, G. Ceder, *Npj Comput. Mater.* **2016**, *2*, 16002.

Manuscript received: June 30, 2023
Revised manuscript received: September 19, 2023
Accepted manuscript online: September 20, 2023

 © 2023 The Authors. Zeitschrift für anorganische und allgemeine Chemie published by Wiley-VCH GmbH

15213749, 2023, 22, Downloaded from https://onlinelibrary.wiley.com/doi/10.1002/zaac.202300146 by Norwegian Institute Of Public Healt Invoice Receipt DFO, Wiley Online Library on [31/01/2024]. See the Terms and Conditions (https://onlinelibrary.wiley.com/terms-and-conditions) on Wiley Online Library for rules of use; OA articles are governed by the applicable Creative Commons License